

---

# MOS: Model Synergy for Test-Time Adaptation on LiDAR-Based 3D Object Detection

---

Zhuoxiao Chen Junjie Meng Mahsa Baktashmotlagh Zi Huang Yadan Luo  
 The University of Queensland  
 {zhuoxiao.chen, junjie.meng, m.baktashmotlagh}@uq.edu.au  
 {helen.huang, y.luo}@uq.edu.au

## Abstract

LiDAR-based 3D object detection is pivotal across many applications, yet the performance of such detection systems often degrades after deployment, especially when faced with unseen test point clouds originating from diverse locations or subjected to corruption. In this work, we introduce a new online adaptation framework for detectors named Model Synergy (MOS). Specifically, MOS dynamically assembles best-fit supermodels for each test batch from a bank of historical checkpoints, leveraging long-term knowledge to guide model updates without forgetting. The model assembly is directed by the proposed synergy weights (SW), employed for weighted averaging of the selected checkpoints to minimize redundancy in the composite supermodel. These weights are calculated by evaluating the similarity of predicted bounding boxes on test data and the feature independence among model pairs in the bank. To maintain an informative yet compact model bank, we pop out checkpoints with the lowest average SW scores and insert newly updated model weights. Our method was rigorously tested against prior test-time domain adaptation strategies on three datasets and under eight types of corruptions, demonstrating its superior adaptability to changing scenes and conditions. Remarkably, our approach achieved a 67.3% increase in performance in a complex “cross-corruption” scenario, which involves cross-dataset inconsistencies and real-world scene corruptions, providing a more realistic testbed of adaptation capabilities. The code is available at <https://github.com/zhuoxiao-chen/MOS>.

## 1 Introduction

Recently, LiDAR-based 3D object detectors have exhibited remarkable performance alongside a diverse array of applications such as robotic systems [1, 40, 85, 74] and self-driving cars [8, 63, 47, 66, 2, 77, 38, 31, 37, 34]. However, when deployed in the real world, the detection system could fail on unseen test data due to unexpectable varying conditions, which is commonly referred to as the *domain shift*. To study this shift, researchers consider cross-dataset scenarios (*e.g.*, from nuScenes [3] to KITTI [12]) where object sizes and beam numbers are varying in the test domain [11, 35, 69], or adding perturbations to clean datasets (*e.g.*, from KITTI to KITTI-C [27]) to mimic realistic corruptions caused by severe weather condition and sensor malfunctions [17, 27, 10]. However, in real-world scenarios, shifts generally does not arise from a unitary source, for example, considering a detection system deployed in an unfamiliar northern city, it is apt to suffer severe weather conditions, such as heavy snow. This leads us to consider a new hybrid shift termed **cross-corruption**, where cross-dataset gaps and corruption noises coexist across 3D scenes (*e.g.*, Waymo [55] to KITTI-C).

These simulated shifts prompt a critical research question: *how can the 3D detector naturally adapt to a shifted target scene?* Previous studies have identified unsupervised domain adaptation (UDA) as a promising solution, by multi-round self-training on the target data with the aid of pseudo-labeling techniques [6, 72, 73, 46, 32], or forcing feature-level alignment between the source and target data for

learning domain-invariant representations [35, 83, 81]. While effective, these UDA-based approaches require an offline training process over **multiple epochs** with pre-collected target samples. Considering a detection system being deployed on a resource-constrained device in the wild, performing such a time-consuming adaptation during testing is **impractical**. To this end, there is an urgent need for a strategy that allows models to adapt to live data streams and provide instant predictions. Test-time Adaptation (TTA) emerges as a viable solution and has been explored in the general classification task, through (1) choosing a small set of network parameters to update (*e.g.*, matching BN statistics [62, 45]) or (2) employing the mean-teacher model to provide consistent supervision [64, 65, 78, 57]. A recent work of MemCLR [61], extends the idea of TTA to image-based 2D object detection by extracting and refining the region of interest (RoI) features for each detected object through a transformer-based memory module.

Despite TTA’s advances in image classification and 2D detection, adapting 3D detection models at test time remains **unexplored**. This motivates us first to conduct a pilot study and investigate the effectiveness of these TTA techniques when applied to 3D detection tasks. As plotted in Fig. 1, methods that employ the mean-teacher model (*e.g.*, MemCLR and CoTTA) outperform the rest of the methods. This superiority stems from the teacher model’s ability to accumulate long-term knowledge, offering stable supervision signals and reducing catastrophic forgetting across batches [26, 18, 21, 29, 25]. However, by treating all previous checkpoints *equally* through moving average (EMA) for each test sample, the teacher model may fail to recap and leverage the most critical knowledge held in different checkpoints. For example, Fig. 2 shows very different characteristics of test point clouds  $x_{t+1}$  and  $x_{t+2}$ , while the teacher model still relies on a uniform set of knowledge (*i.e.*, generated by EMA), without leveraging relevant insights from prior checkpoints tailored to each specific scene. Hence, there is no teacher model perfectly fitting all target samples. We argue that an optimal “super” model should be dynamically assembled to accommodate each test batch.

In this paper, we present a Model Synergy (MOS) strategy that adeptly selects and assembles the most suitable prior checkpoints into a unified super model, leveraging long-term information to guide the supervision for the current batch of test data. To this end, we introduce the concept of synergy weights (SW) to facilitate the model assembly through a weighted averaging of previously trained checkpoints. A model synergy bank is established to retain  $K$  previously adapted checkpoints. As illustrated in Fig. 2, to assemble a super model tailored to test batch  $x_{t+1}$ , checkpoints 1 and 3 are assigned lower SW due to redundant box predictions. To leverage the knowledge uniquely held by checkpoint 4 (*e.g.*, concepts about cyclist and pedestrians), MOS assigns it with a higher SW.

To determine the optimal SW for the ensemble, we reformulate this as solving a linear equation, intending to create a super model that is both diverse and exhibits an equitable level of similarity to all checkpoints, without showing bias towards any. The closed-form solution of this linear equation leads to calculating the inverse Gram matrix, which quantifies the similarity between checkpoint pairs. To this end, we devise two similarity functions tailored for 3D detection models from 1) output-level, measuring prediction discrepancies through Hungarian matching cost of 3D boxes, and 2) feature-level, assessing feature independence via calculating the matrix rank of concatenated feature maps. By computing these similarities for each new test batch, we determine the SW for the construction of the super model. This super model then generates pseudo labels, which are employed to train the model at the current timestamp for a single iteration.

However, with more saved checkpoints during test-time adaptation, the memory cost significantly increases. To address this, we introduce a dynamic model update strategy that adds new checkpoints, while simultaneously removing the least important ones. Empirical results evidence that our approach, which maintains only 3 checkpoints in the model bank, outperforms the assembly of the 20 latest checkpoints and reduces memory consumption by 85%. The **contribution** of this paper is summarized as follows:

1. This is an early attempt to explore the test-time adaptation for LiDAR-based 3D object detection (TTA-3OD). In addressing the challenges inherent to TTA-3OD, we propose a

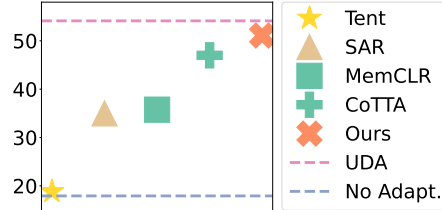


Figure 1: The results (AP<sub>3D</sub>) of applying existing TTA methods to adapt the 3D object detector [71] from nuScenes to KITTI. Mean-teacher models are in green.

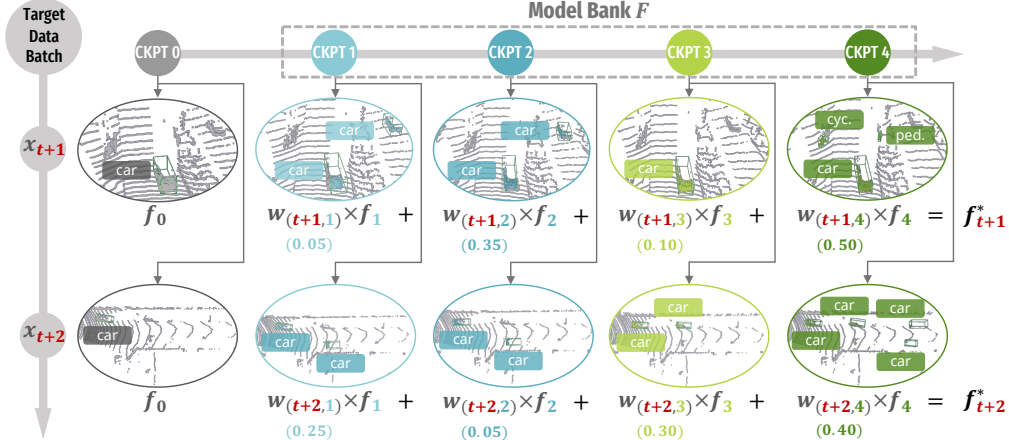


Figure 2: Illustration of the **model synergy (MOS)** that selects key checkpoints and assembles them into a **super model  $f_{t+1}^*$**  that **tailors for each of test data  $x_{t+1}$** . “cyc.” denotes the cyclist and “ped.” denotes the pedestrian. MOS prioritizes checkpoints with *unique* insights that are absent in other checkpoints with *higher* weights while reducing the weights of those with redundant knowledge.

novel Model Synergy (MOS) approach to dynamically leverage and integrate collective knowledge from historical checkpoints.

2. Unlike mean-teacher based methods that aggregate all previous checkpoints, we identify and assemble the most suitable ones according to each test batch. To this end, we utilize the inverse of the generalized Gram matrix to determine the weights. We introduce similarity measurements for 3D detection models at both feature and output levels to calculate the generalized Gram matrix.
3. We conduct comprehensive experiments to address real-world shifts from (1) cross-dataset, (2) corrupted datasets, and (3) hybrid cross-corruption scenarios including eight types of simulated corruptions. Extensive experiments show that the proposed MOS even outperforms the UDA method, which requires multi-round training, when adapting from Waymo to KITTI. In a more challenging scenario of cross-corruption, MOS surpasses the baseline and direct inference by 67.3% and 161.5%, respectively.

## 2 Related Work

**Domain Adaption for 3D Object Detection** aims to transfer knowledge of 3D detectors, from labeled source point clouds to an unlabeled target domain, by mitigating the domain shift across different 3D scenes. The shift in 3D detection is attributed to variations in many factors such as object statistics [67, 60], weather conditions [70, 17], sensor differences [49, 16, 69], sensor failures [27], and the synthesis-to-real gap [50, 7, 30]. To bridge these gaps, approaches including adversarial matching of features [83], the generation of enhanced 3D pseudo labels [72, 73, 6, 51, 76, 33, 46, 22, 59], the mean-teacher model [35, 19] for stable adaptation, and contrastive learning [81] for tighter embeddings have been extensively investigated. However, implementing these cross-domain methods necessitates multiple epochs of retraining, rendering them impractical for scenarios where test data arrives in a streaming manner.

**Test-Time Adaptation (TTA)** seeks to adapt the model to unseen data at inference time, by addressing domain shifts between training and test data [68]. A very first work, Tent [62] leverages entropy minimization to adjust batch norm parameters. Subsequently, many works have adopted similar approaches of updating a small set of parameters, each with different strategies and focuses [44, 39, 13, 78, 84, 43, 14, 45, 20, 53, 42, 43]. For instance, EATA [44] identifies reliable, non-redundant samples to optimize while DUA [39] introduces adaptive momentum in a new normalization layer. NOTE [13] updates batch norms at the instance level, whereas RoTTA [78] and DELTA [84] leverage global statistics for batch norm updates. Additionally, SoTTA [14] and SAR [45] enhance batch norm optimization through sharpness-aware minimization. Alternatively, some approaches optimize the entire network through the mean-teacher framework for stable supervision [64, 58], generating reliable pseudo labels for self-training [15, 80], employing feature clustering [5, 23, 65], and utilizing

augmentations to enhance model robustness [82]. Despite these TTA methods being developed for general image classification, MemCLR [61] is the pioneering work applying TTA for image-based 2D object detection, utilizing a mean-teacher approach for aligning instance-level features. Nevertheless, the applicability of these image-based TTA methods to object detection from 3D point clouds is remains unexplored.

### 3 Proposed Approach

#### 3.1 Problem Definition

In this section, we establish the definition and notations for the Test-Time Adaptation for 3D Object Detection (TTA-3OD). When deploying a 3D detection model pretrained on a source dataset, the test point clouds  $\{x_t\}_{t=1}^T$  are shifted or/and corrupted due to varying real-world conditions, where  $x_t$  is the  $t$ -th test point cloud in the stream of test data. The ultimate goal of TTA-3OD is to adapt the 3D detection model to a sequence of target scenes in a single pass during the inference time.

#### 3.2 Overall Framework

The core idea of our methodology is to identify the most suitable historical models with distinct knowledge for each test batch  $x_t$ , and assemble them into a **super model**  $f_t^*$  facilitating the model adaptation during the test time. To this end, we establish a model bank  $\mathbf{F} = \{f_1, \dots, f_K\}$  of size  $K$  to preserve and synergize the previously trained models. The overall workflow of our method unfolds in three phases, as cleared shown in Fig. 3 and Algorithm 1 (in Appendix).

**Phase 1: Warm-up** Initially, when the model bank  $\mathbf{F}$  is not yet populated, we train the model with first  $K$  arriving target batches by pseudo labeling-based self-training. We save the model as a checkpoint at each timestamp,  $\{f_1, \dots, f_K\}$ , into the  $\mathbf{F}$  until reaching its capacity of  $K$ .

**Phase 2: Model Synergy** Once  $\mathbf{F}$  is full, for every subsequent test batch  $x_t$ , checkpoints within  $\mathbf{F}$  are assembled into a super model  $f_t^*$  to provide pseudo labels  $\hat{\mathbf{B}}^t$  for supervision. For instance, as illustrated in phase 2 of Fig. 3, when inferring  $x_{K+1}$ , we assemble the super model via  $\mathbf{F}$  into  $f_{K+1}^* = w_{(K+1,1)}f_1 + \dots + w_{(K+1,K)}f_K$ . Then, pseudo labels  $\hat{\mathbf{B}}^{K+1}$  are generated by  $f_{K+1}^*$  to train the current model  $f_{K+1}$  for a single iteration. When  $L$  batches are tested, we update the model bank.

**Phase 3: Model Bank Update** To maintain a compact model bank  $\mathbf{F}$ , meanwhile, each model holds distinct knowledge, we dynamically update the bank  $\mathbf{F}$  to fix its size at  $K$ . For every  $L$  batches tested, we replace the checkpoint with the most redundant knowledge in  $\mathbf{F}$ , with the newly trained  $f_t$ . Phases 2 and 3 alternate until all target samples  $\{x_t\}_{t=1}^T$  have been tested.

#### 3.3 Model Synergy

As phase 1 is straightforward, where the model bank is filled up with the first  $K$  checkpoints, we elaborate on the details of Phase 2 in this subsection. An intuitive example is presented in Fig. 2: when inferring a target point cloud, different historical models yield inconsistent predictions because these models learned characteristics from different batches at earlier timestamps. However, if these characteristics no longer appear in subsequent arriving test data, the model may suffer catastrophic forgetting, losing previously learned information. Our strategy to overcome this, is to leverage and combine the long-term knowledge from prior checkpoints. But, not all checkpoints are equally important, as shown in Fig. 2, checkpoints 1 and 2 produce highly similar box predictions, whereas checkpoint 4 can detect objects that are missed by others. Treating these checkpoints equally leads to the accumulation of redundant information. Therefore, we propose synergy weights (SW) to emphasize unique insights and minimize knowledge redundancy, via weighted averaging of the historical checkpoints. Ideally, similar checkpoints (e.g., CKPT 1 and 2 in Fig. 2) should be assigned with *lower* SW, whereas the checkpoint exhibits unique insights (e.g., CKPT 4 in Fig. 2) should

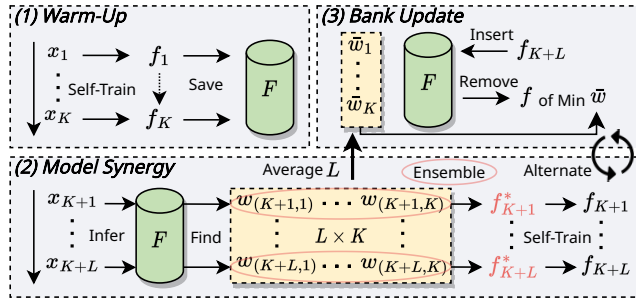


Figure 3: The overall workflow of our approach.

be rewarded with *higher* SW. Through weighting each checkpoint, we linearly assemble them into an super model  $f_t^*$  that best fits the current test batch  $x_t$ . In the following section, we discuss our approach to determine these optimal SW for the super model ensemble.

### 3.3.1 Super Model Ensemble by Optimal Synergy Weights

For each batch  $x_t$ , we assume there exist optimal synergy weights  $\mathbf{w} \in \mathbb{R}^K$  for linearly assembling the historical checkpoints within the model bank  $\mathbf{F}$  into a super model  $f_t^*$  as below:

$$\mathbf{F}\mathbf{w} = f_t^*. \quad (1)$$

For simplicity, we use the same notation  $f_t$  to indicate the model parameters. The optimal synergy weights  $\mathbf{w}$  can be deduced by solving the linear equation:

$$\mathbf{w} = (\mathbf{F}^T \mathbf{F})^{-1} \mathbf{F}^T f_t^*, \quad (2)$$

which can be decomposed into two parts, (1)  $(\mathbf{F}^T \mathbf{F})^{-1}$ : inverse of the Gram matrix, and (2)  $\mathbf{F}^T f_t^*$ : pairwise similarities between each model in  $\mathbf{F}$  and the super model  $f_t^*$ . Ideally, these similarities are expected to be uniformly distributed, ensuring  $f_t^*$  remains unbiased towards any single model in  $\mathbf{F}$  for a natural fusion of diverse, long-term knowledge. Thus, we can simplify the Eq. (2) as:

$$\mathbf{w} = (\mathbf{F}^T \mathbf{F})^{-1} \mathbb{1}^K. \quad (3)$$

Now, to compute the optimal synergy weights  $\mathbf{w}$ , we delve into the first part of Eq. (3) to compute the Gram matrix  $\mathbf{G} = \mathbf{F}^T \mathbf{F}$  which captures the model parameter similarity for any arbitrary pair of models  $(f_i, f_j)$  in the bank  $\mathbf{F}$ , as:

$$\mathbf{G} = \mathbf{F}^T \mathbf{F} = \left( \langle f_i, f_j \rangle \right)_{i,j=1}^K \in \mathbb{R}^{K \times K}, f_i, f_j \in \mathbf{F}, \quad (4)$$

where  $\langle f_i, f_j \rangle$  denotes the inner product of the model parameters of  $f_i$  and  $f_j$ . Based on the similarities captured in  $\mathbf{G}$ , its inverse,  $\mathbf{G}^{-1}$ , essentially prioritizes directions of higher variance (diverse information) and penalizes directions of lower variance (duplicated information). Thus, the synergy weights calculated by  $\mathbf{w} = \mathbf{G}^{-1} \mathbb{1}^K$ , are theoretically low for those checkpoints with knowledge duplicates. Previous studies [9, 79, 41] have also demonstrated the effectiveness of using the  $\mathbf{G}^{-1}$  to determine importance weights.

### 3.3.2 Inverse of Generalized Gram Matrix for 3D Detection Model

While the inverse of the Gram matrix is effective, evaluating similarity through the inner product of model parameters  $f_i$  and  $f_j$  is suboptimal, as models with *distinct* parameters may produce *similar* predictions on the same input test batch  $x_t$ . Hence, tailored to each input batch  $x_t$ , we compare intermediate features and final box predictions outputted by a pair of the models  $(f_i, f_j)$ . To this end, we propose a feature-level similarity function  $\mathcal{S}_{\text{feat}}(\cdot; \cdot)$  and an output-level box set similarity function  $\mathcal{S}_{\text{box}}(\cdot; \cdot)$  to effectively quantify the discrepancy between any two 3D detection models (will be discussed in next section). By substituting the inner product with the proposed similarity functions, the original Gram matrix  $\mathbf{G}$  evolves into a generalized version  $\tilde{\mathbf{G}}$ , especially designed for 3D detectors. By combing Eq. (3) and (4), we can calculate the  $\tilde{\mathbf{G}}$  and the optimal synergy weights  $\tilde{\mathbf{w}}$  as:

$$\tilde{\mathbf{w}} = (\mathbf{F}^T \mathbf{F})^{-1} \mathbb{1}^K = \tilde{\mathbf{G}}^{-1} \mathbb{1}^K, \tilde{\mathbf{G}} = \left( \mathcal{S}_{\text{box}} \langle f_i, f_j \rangle \times \mathcal{S}_{\text{feat}} \langle f_i, f_j \rangle \right)_{i,j=1}^K, \quad (5)$$

where each element represents the feature and prediction similarity between each pair of historical 3D detection models  $(f_i, f_j)$  in  $\mathbf{F}$ . Next, the super model  $f_t^*$  is linearly aggregated by all historical checkpoints  $\mathbf{F} \in \mathbb{R}^K$  weighted by  $\tilde{\mathbf{w}} \in \mathbb{R}^K$  as follows:

$$f_t^* = \sum_{i=1}^K w_i f_i, w_i \in \tilde{\mathbf{w}}, f_i \in \mathbf{F}, \quad (6)$$

where the synergized **super model**  $f_t^*$  is used to guide supervision of the current model  $f_t$ . As illustrated in Fig. 3, for the test sample at time  $t$ , assembled  $f_t^*$  generates the stable pseudo labels  $\hat{\mathbf{B}}^t$  to train  $f_{t-1} \rightarrow f_t$  with a single iteration, as below:

$$\hat{\mathbf{B}}^t \leftarrow f_t^*(x_t), f_t \xleftarrow{\text{train}} \text{aug}(x_t, \hat{\mathbf{B}}^t), \quad (7)$$

where  $\text{aug}(\cdot, \cdot)$  indicates data augmentation applied to the pseudo-labeled target point clouds. Recall Eq. (5), the key to finding the optimal synergy weights is to accurately measure the similarities of the features and outputs between a pair of 3D detection models. For each test batch  $x_t$ , we utilize the intermediate feature map  $\mathbf{z}_t$  and the final box prediction set  $\mathbf{B}^t$  outputted by modern 3D detectors [75, 28, 47, 36] for similarity measurement. We introduce a feature-level similarity function  $\mathcal{S}_{\text{feat}}(\cdot; \cdot)$  to assess feature independence between intermediate feature maps  $(\mathbf{z}_i, \mathbf{z}_j)$ , and an output-level similarity function  $\mathcal{S}_{\text{out}}(\cdot; \cdot)$  to gauge the discrepancy in box predictions  $(\mathbf{B}^i, \mathbf{B}^j)$ , where  $(\mathbf{z}_i, \mathbf{z}_j)$  and  $(\mathbf{B}^i, \mathbf{B}^j)$  are generated by any pair of models  $(f_i, f_j)$  within the model bank  $\mathbf{F}$ .

### 3.3.3 Feature-Level Similarity $\mathcal{S}_{\text{feat}}$

To assess the similarity between feature maps  $(\mathbf{z}_i, \mathbf{z}_j)$ , we utilize the rank of the feature matrix to determine linear independencies among the feature vectors in  $\mathbf{z}_i$  relative to those in  $\mathbf{z}_j$ . Each single feature vector in the feature map, encodes the information of a small receptive field within the 3D scene. When inferring the input batch  $x_t$ , if a feature vector in  $\mathbf{z}_i$  is linearly independent from the other in  $\mathbf{z}_j$ , it means  $\mathbf{z}_i$  and  $\mathbf{z}_j$  are either capturing information from distinct receptive fields, or focusing the same region but interpreting differently. To calculate such independencies, we concatenate the feature maps  $\mathbf{z}_i \oplus \mathbf{z}_j$  and calculate its  $\text{rank}(\cdot)$ , which identifies the maximum number of linearly independent feature vectors. A *higher* rank of  $\mathbf{z}_i \oplus \mathbf{z}_j$  signifies a *greater diversity* of features, because *fewer* feature vectors can be linearly combined by others. To accelerate the computation, we approximate the  $\text{rank}(\cdot)$  by computing the nuclear norm of the feature matrix [48, 24]. With the input batch  $x_t$ , the feature-level similarity  $\mathcal{S}_{\text{feat}}$  between a pair of detection models  $(f_i, f_j)$ , can be determined as follows:

$$\mathcal{S}_{\text{feat}}(f_i, f_j) = 1 - \frac{\text{rank}(\mathbf{z}_i \oplus \mathbf{z}_j)}{D}, \quad \mathbf{z}_i, \mathbf{z}_j \in \mathbb{R}^{2HW \times D}, \quad (8)$$

where  $\mathbf{z}_i, \mathbf{z}_j$  are the feature maps generated by  $f_i$  and  $f_j$ , respectively.  $H, W, D$  denote the height, width, dimension of the feature map, and  $D$  is the maximum possible value of  $\text{rank}(\cdot)$ .  $\mathcal{S}_{\text{feat}}$  falls within the range from 0 to 1, and a *higher* value of  $\mathcal{S}_{\text{feat}}$  indicates *less* feature independence between  $\mathbf{z}_i$  and  $\mathbf{z}_j$ , resulting in *more similar* feature maps yielded by models  $f_i$  and  $f_j$ .

### 3.3.4 Output-level Box Similarity $\mathcal{S}_{\text{box}}$

To assess the similarity between box predictions  $(\mathbf{B}^i, \mathbf{B}^j)$ , we treat it as a *set matching* problem, since  $\mathbf{B}^i$  and  $\mathbf{B}^j$  represent sets of predicted bounding boxes that can vary in size. To solve it, we apply the Hungarian matching algorithm [4, 54], a robust method for bipartite matching that ensures the best possible one-to-one correspondence between two sets of box predictions. We extend the smaller box set with  $\emptyset$  to equalize the sizes of both sets to  $N$ . To determine an optimal bipartite matching between these two equal-sized sets, the Hungarian algorithm is used to find a permutation of  $N$  elements:  $p \in \mathbf{P}$ , which yields the lowest cost:

$$\tilde{p} = \arg \min_{p \in \mathbf{P}} \sum_n \mathcal{L}_{\text{box}}(\mathbf{B}_n^i; \mathbf{B}_{p(n)}^j), \quad (9)$$

where  $\mathbf{B}_n^i$  is  $n$ -th box in the set  $\mathbf{B}^i$  predicted by the model  $f_i$ . The box loss  $\mathcal{L}_{\text{box}}(\cdot; \cdot)$  is calculated by the intersection-over-union (IoU) plus the L1 distance covering the central coordinates, dimensions, and orientation angles between a pair of boxes:  $\mathbf{B}_n^i$  and its corresponding box indexed by  $p(n)$ . The indicator function  $\mathbb{1}_{\{c_n^i \neq \emptyset\}}$  means the cost is calculated only when the category of  $n$ -th object is not the padded  $\emptyset$ . The next step is to compute the total Hungarian loss [4] for all pairs of matched boxes:

$$\mathcal{S}_{\text{box}}(f_i, f_j) = \left( \sum_{n=1}^N \mathbb{1}_{\{c_n^i \neq \emptyset\}} \mathcal{L}_{\text{box}}(\mathbf{B}_n^i; \mathbf{B}_{\tilde{p}(n)}^j) \right)^{-1}, \quad (10)$$

where  $\tilde{p}$  is the optimal assignment computed in the Eq. (9). We normalize the result to the same range as  $\mathcal{S}_{\text{feat}}$  using a sigmoid function. A *higher* value of  $\mathcal{S}_{\text{box}}$  indicates that models  $f_i$  and  $f_j$  predict *more overlapping* boxes.

## 3.4 Model Bank Update

In TTA-3OD, with increasing number of test batches, simply inserting checkpoints at all timestamps to the model bank  $\mathbf{F}$  results in substantial memory cost and knowledge redundancy. As observed from our empirical results (Fig. 6), assembling the latest 20 checkpoints yields similar

Table 1: Results of test-time adaptation for 3D object detection across different datasets. We report  $AP_{BEV} / AP_{3D}$  in moderate difficulty. Oracle mean fully supervised training on the target dataset. We indicate the best adaptation result by **bold**.

Method	Venue	TTA	Waymo $\rightarrow$ KITTI		nuScenes $\rightarrow$ KITTI	
			$AP_{BEV} / AP_{3D}$	Closed Gap	$AP_{BEV} / AP_{3D}$	Closed Gap
No Adapt.	-	-	67.64 / 27.48	-	51.84 / 17.92	-
SN [67]	CVPR'20	$\times$	78.96 / 59.20	+72.33% / +69.00%	40.03 / 21.23	+37.55% / +5.96%
ST3D [72]	CVPR'21	$\times$	82.19 / 61.83	+92.97% / +74.72%	75.94 / 54.13	+76.63% / +65.21%
Oracle	-	-	83.29 / 73.45	-	83.29 / 73.45	-
Tent [62]	ICLR'21	$\checkmark$	65.09 / 30.12	-16.29% / +5.74%	46.90 / 18.83	-15.71% / +1.64%
CoTTA [64]	CVPR'22	$\checkmark$	67.46 / 35.34	-1.15% / +17.10%	68.81 / 47.61	+53.96% / +53.47%
SAR [45]	ICLR'23	$\checkmark$	65.81 / 30.39	-11.69% / +6.33%	61.34 / 35.74	+30.21% / +32.09%
MemCLR [61]	WACV'23	$\checkmark$	65.61 / 29.83	-12.97% / +5.11%	61.47 / 35.76	+30.62% / +32.13%
<b>MOS</b>	-	$\checkmark$	<b>81.90 / 64.16</b>	<b>+91.12% / +79.79%</b>	<b>71.13 / 51.11</b>	<b>+61.33% / +59.78%</b>

performance to assembling only the latest 5 checkpoints. Hence, our goal is to make the  $\mathbf{F}$  retain only a minimal yet highly diverse set of checkpoints. To this end, we regularly update the model bank, by adding new models and removing redundant ones every time  $L$  online batches are inferred. As illustrated in Fig. 3, upon adapting every  $L$  samples  $\{x_l, x_{l+1}, \dots, x_L\}$ , a single checkpoint  $f_i \in \mathbf{F}$  engages in the assembly  $L$  times, thereby  $L$  synergy weights are calculated and stored into a list  $\{w_{(l,i)}, w_{(l+1,i)}, \dots, w_{(L,i)}\}$ . Given  $K$  checkpoints in  $\mathbf{F}$ , a synergy matrix is defined as  $\mathbf{W} = (w_{(l,k)})_{l=1, k=1}^{L, K} \in \mathbb{R}^{L \times K}$ . After inferring  $L$  batches, we average across the  $L$  dimension to calculate the mean synergy weight for each checkpoint, denoted as:

$$\bar{\mathbf{w}} = \{\bar{w}_1, \dots, \bar{w}_K\} \in \mathbb{R}^K. \quad (11)$$

Finally, we remove the model with **the lowest** mean synergy weight in  $\bar{\mathbf{w}}$  and add the current model  $f_t$  to the bank as follows:

$$\mathbf{F} \leftarrow \mathbf{F} \setminus \{f_i\}, i = \text{index}(\bar{\mathbf{w}}; \min(\bar{\mathbf{w}})), \mathbf{F} \leftarrow \mathbf{F} \cup \{f_t\}, \quad (12)$$

where  $i$  denotes the index of the minimum mean synergy weight in  $\bar{\mathbf{w}}$ . By updating the model bank this way, we maintain a fixed number of  $K$  checkpoints in  $\mathbf{F}$ , each carrying unique insights.

## 4 Experiments

### 4.1 Experimental Setup

**Datasets and TTA-3OD Tasks.** We perform extensive experiments across three widely used LiDAR-based 3D object detection datasets: **KITTI** [12], **Waymo** [55], and **nuScenes** [3], along with a recently introduced dataset simulating real-world corruptions, **KITTI-C** [27] for TTA-3OD challenges. We firstly follow [72, 73, 6] to tackle cross-dataset test-time adaptation tasks (e.g. Waymo  $\rightarrow$  KITTI and nuScenes  $\rightarrow$  KITTI-C), which include adaptation (i) across object shifts (e.g., scale and point density), and (ii) across environmental shifts (e.g., deployment locations and LiDAR beams). We also conduct experiments to tackle a wide array of real-world corruptions (e.g., KITTI  $\rightarrow$  KITTI-C) covering: Fog, Wet Conditions (Wet.), Snow, Motion blur (Moti.), Missing beams (Beam.), Crosstalk (Cross.T), Incomplete echoes (Inc.), and Cross-sensor (Cross.S). Finally, we address the hybrid shift cross-corruptions (e.g., Waymo  $\rightarrow$  KITTI-C), where cross-dataset inconsistency and corruptions coexist in test scenes. The implementation details are included in Appendix A.1.

**Baseline Methods.** We compare the proposed method using voxel-based backbone (e.g., SECOND) with a diverse range of baseline methods: (i) **No Adapt.** refers to the model pretrained from the source domain, directly infer the target data; (ii) **SN** [67] is a *weakly supervised domain adaptation* method for 3D detection by rescaling source object sizes with target statistics for training; (iii) **ST3D** [72] is the pioneering *unsupervised domain adaptation* method for 3D detection with multi-epoch pseudo labeling-based self-training; (iv) **Tent** [62] is an *online TTA* method which optimizes the model by minimizing entropy of its prediction; (v) **CoTTA** [64] is an *online TTA* approach which employs mean-teacher to provide supervision with augmentations and restores neurons to preserve knowledge; (vi) **SAR** [45] improves Tent by sharpness-aware and reliable entropy minimization for *online TTA*; (viii) **MemCLR** [61] is the first work for *online adaptation on image-based object detection*, by utilizing mean-teacher to align the instance-level features with a memory module; (ix) **Oracle** means a *fully supervised* model trained on the target domain.

Table 2: Results of test-time adaptation for 3D object detection across different corruptions (KITTI → KITTI-C) at heavy level. AP<sub>3D</sub> at easy/moderate/hard difficulty of KITTI metric are reported.

	No Adaptation	Tent [62]	CoTTA [64]	SAR [45]	MemCLR [61]	MOS
Fog	84.66/72.85/68.23	85.11/73.02/68.73	85.10/72.94/68.49	84.64/ 72.52/68.14	84.71/72.70/68.23	<b>85.22/74.02/69.11</b>
Wet.	88.23/78.82/76.25	88.13/78.79/76.36	88.27/79.02/76.43	88.11/78.60/76.23	88.04/78.68/76.25	<b>89.32/81.91/77.79</b>
Snow	71.11/63.92/59.07	71.71/64.48/59.50	71.83/64.59/59.45	72.29/64.08/58.78	72.33/63.84/58.74	<b>75.07/67.87/62.72</b>
Moti.	43.35/39.23/38.21	43.02/39.15/38.15	44.48/39.68/38.62	42.89/39.13/38.12	42.86/38.44/37.57	<b>44.70/41.63/40.59</b>
Beam.	75.42/57.49/53.93	76.62/58.01/53.85	76.39/57.50/53.98	75.98/57.67/53.75	75.70/57.48/53.49	<b>78.74/60.48/55.91</b>
CrossT.	87.98/78.46/ <b>75.49</b>	87.62/77.92/74.67	86.78/76.05/72.22	87.74/77.59/74.51	86.20/77.11/74.25	<b>89.22/79.10/75.47</b>
Inc.	46.98/30.33/25.68	47.82/30.87/26.44	49.92/32.77/27.85	47.27/30.46/26.42	49.99/32.08/27.47	<b>59.13/40.29/34.53</b>
CrossS.	68.44/47.37/41.08	68.89/46.75/41.17	69.15/47.11/40.80	68.17/46.45/40.63	69.17/47.28/40.90	<b>71.87/49.28/43.68</b>
Mean	70.77/58.56/54.74	71.11/58.62/54.86	71.49/58.71/54.73	70.89/58.31/54.57	71.13/58.45/54.61	<b>74.16/61.82/57.48</b>

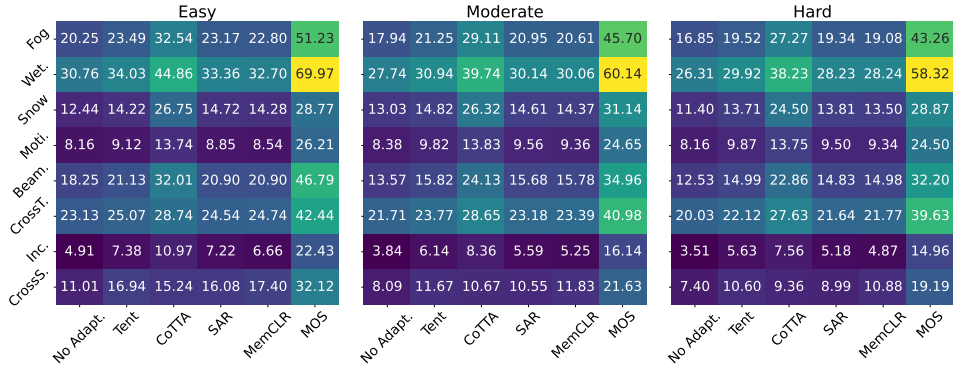


Figure 4: Heatmap intuitively presenting the results of TTA-3OD across hybrid cross-corruption shifts (Waymo → KITTI-C) in heavy difficulty. Darker/lighter shades indicate lower/higher performance. We report AP<sub>3D</sub> across all difficulties levels.

## 4.2 Main Results and Analysis

We present and analyze the main results of car detection using SECOND [71] as the backbone 3D detector, when comparing the proposed MOS against baseline methods across three types of domain shifts. The results of additional object classes are detailed in the Appendix A.2, and the examination of alternative backbone detectors (*e.g.*, PVRCNN [52]), is presented in the Appendix A.4.

**Cross-dataset Shifts.** We conducted comprehensive experiments on two cross-dataset 3D adaptation tasks, as reported in Tab 1, when compared to the best TTA baseline CoTTA [64], the proposed MOS consistently improves the performance in Waymo → KITTI and nuScenes → KITTI tasks by a large margin of 81.5% and 7.4% in AP<sub>3D</sub>, respectively. This improvement significantly closes the performance gap (91.12% and 79.79%) between No Adapt. and Oracle. Remarkably, the proposed MOS outperforms the UDA method ST3D [72], which requires multi-epoch training: MOS’s 64.16% vs. ST3D’s 61.83% in AP<sub>3D</sub>, and even demonstrates comparable performance to the upper bound performance (Oracle): MOS’s 81.90% vs. Oracle’s 83.29% in AP<sub>BEV</sub> when adapting to Waymo.

**Corruption Shifts.** We carry out comprehensive experiments (KITTI → KITTI-C) across eight different types of real-world corruptions to validate the effectiveness of the proposed MOS to mitigate these corruption shifts. As reported in Tab. 2, MOS surpasses all TTA baselines across every type of corruption, achieving AP<sub>3D</sub> gains of 3.73%, 5.56%, and 4.78% at easy, moderate, and hard levels, respectively. Notably, MOS greatly addresses the most severe shift caused by incomplete echoes, improving 23.98% at the hard difficulty level. These promising results highlight MOS’s robustness to adapt 3D models to various corrupted scenarios, particularly those challenging ones.

**Cross-corruption Shifts.** To address the hybrid shifts where cross-dataset discrepancies and corruptions simultaneously occur, we conduct experiments to adapt 3D detectors from Waymo to KITTI-C. We visualize the results utilizing the heatmap (in Fig. 4). It is observed that the shades in the last column (MOS), are significantly lighter than those in all other columns (TTA baselines), indicating the superior performance of MOS over all other methods. It is worth noting that, the

Figure 5: Ablative study of the proposed MOS on Waymo → KITTI. The best result is highlighted in **bold**.

Ablation	AP <sub>3D</sub>			AP <sub>BEV</sub>		
	Easy	Moderate	Hard	Easy	Moderate	Hard
w/o Ensemble	45.17	43.14	41.48	71.36	68.17	68.96
Mean Ensemble	48.56	45.89	44.37	72.72	70.34	70.15
MOS w/o S <sub>feat</sub>	67.02	59.98	58.76	91.85	81.90	79.77
MOS w/o S <sub>box</sub>	72.99	61.40	60.09	88.52	80.15	79.06
MOS	<b>74.09</b>	<b>64.16</b>	<b>62.33</b>	<b>91.85</b>	<b>81.90</b>	<b>81.78</b>



results without any adaptation (column 1) remarkably degrade, due to the challenging hybrid shifts, for example, only 3.51% for incomplete echoes and 7.40% for cross-sensor at a hard level. Our approach greatly enhances adaptation performance for these two challenging corruptions by **97.99%** and **76.38%**, respectively, compared to the best baselines. Thus, prior TTA baselines fail to mitigate the significant domain shifts across 3D scenes, whereas the proposed MOS successfully handles various cross-corruption shifts, surpassing the highest baseline and direct inference by **67.3%** and **161.5%**, respectively, across all corruptions.

### 4.3 Ablation and Sensitivity Study

**Ablation Study.** To validate the effectiveness of each component in the proposed MOS, we conduct ablation experiments on Waymo  $\rightarrow$  KITTI and report the  $AP_{3D}$  across three difficulty levels. First, we remove the pivotal component in our method, model assembly, opting instead to simply use the model at the current timestamp for pseudo-label generation. Tab. 5 shows that without assembly (row 1), the adaptation yields suboptimal results, achieving only 43.14% in moderate  $AP_{3D}$ . Then we assemble the recent five checkpoints by averaging their parameters (row 2), and observe a marginal improvement in moderate  $AP_{3D}$  to 45.89%. While our proposed assembly strategy (row 5), identifying and assembling the most useful 5 checkpoints through weighted averaging, significantly outperforms average aggregation by 39.8%. Next, we remove each of the proposed similarity functions used to calculate the synergy weights for the model ensemble. As shown in Tab. 5, removing either  $S_{\text{feat}}(\cdot; \cdot)$  or  $S_{\text{box}}(\cdot; \cdot)$  leads to a notable decrease in moderate  $AP_{3D}$  by 6.9% and 4.5%, respectively, proving that both functions accurately gauge similarity between any pair of 3D detection models.

**Sensitivity to Hyperparameters.** In this section, we examine how the adaptation performance of the proposed MOS is affected by the hyperparameters  $L$  and  $K$ , which determines the period of the model bank update (*i.e.*, every  $L$  batches of test data) and the bank capacity. To study  $L$ , we conduct experiments with values ranging from 64 to 128. As illustrated in the Fig. 6 (*left*), the  $AP_{\text{BEV}}$  (blue curve) remains stable, while the  $AP_{3D}$  (green curve) increases as  $L$  grows from 64 to 96. This occurs because a larger  $L$  reduces the model update frequency, enabling the model bank to retain older checkpoints that hold distinct long-term knowledge. Upon reaching 96,  $AP_{3D}$  becomes stable with a slight fluctuation of 1.67%.

To assess the informativeness and significance of the  $K$  checkpoints selected by the proposed MOS, we developed a comparative analysis between the standard MOS and a simplified variant: *latest-first* MOS. This variant (crosses in Fig. 6 *right*) utilizes the most recent  $K$  checkpoints and employs the same ensemble strategy as MOS (*i.e.*, Eq. (5) and (6)). The standard MOS, that maintains  $K$  checkpoints with high synergy weights (SW) (Sec. 3.4), is referred to as SW-first MOS (stars in Fig. 6 *right*). As shown in Fig. 6, latest-first MOS presents an obvious improvement in  $AP_{3D}$  from 43.14% to 54.18% and in  $AP_{\text{BEV}}$  from 68.17% to 76.29% when assembling more latest checkpoints ( $K$  increases from 1 to 5). However, expanding the ensemble to 20 models yields a marginal increase to 56.16% in  $AP_{3D}$  and 77.54% in  $AP_{\text{BEV}}$ , with a substantial memory cost. The SW-first MOS, which dynamically utilizes only 3 historical checkpoints based on averaged SW, outperforms latest-first MOS with 20 checkpoints by 18.42% in  $AP_{3D}$  and 5.84% in  $AP_{\text{BEV}}$ , meanwhile, reducing memory usage by 85%. This efficiency highlights our method’s ability to selectively keep the most pivotal historical models in the model bank, optimizing both detection performance and memory expenditure.

## 5 Conclusion

This paper is an early attempt to explore the test-time adaptation for LiDAR-based 3D object detection and introduces an effective model synergy approach that leverages long-term knowledge from historical checkpoints to tackle this task. Comprehensive experiments and analysis confirm that the proposed approach efficiently adapts both voxel-based and point-based 3D detectors to various scenes in a single pass at test time, effectively addressing real-world domain shifts sourced from cross-dataset, corruptions, and cross-corruptions. The main limitation of the proposed method is

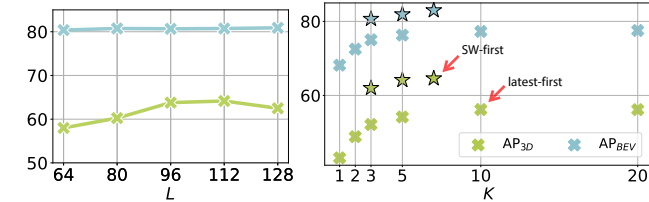


Figure 6: *Left*: Sensitivity to the period of model bank update  $L$ . *Right*: Comparison between two MOS-based ensemble strategies (SW-first vs. latest-first) with increasing model bank size  $K$ . Both  $AP_{\text{BEV}}$  and  $AP_{3D}$  are plotted when adapting the 3D detector [71] from Waymo [55] to KITTI [12].

its high computational demand. Appendix A.5 provides a detailed analysis of this issue, covering algorithm complexity and actual resource usage. Future efforts will focus on improving the time and space efficiency of the algorithm, through storing, and assembly of only a small portion of model parameters (*e.g.*, selected layers or modules) to facilitate faster adaptation at test time.

## References

- [1] Ahmed, S.M., Tan, Y.Z., Chew, C., Mamun, A.A., Wong, F.S.: Edge and corner detection for unorganized 3d point clouds with application to robotic welding. In: Proc. International Conference on Intelligent Robots and Systems (IROS). pp. 7350–7355 (2018)
- [2] Arnold, E., Al-Jarrah, O.Y., Dianati, M., Fallah, S., Oxtoby, D., Mouzakitis, A.: A survey on 3d object detection methods for autonomous driving applications. *IEEE Transactions on Intelligent Transportation Systems* **20**(10), 3782–3795 (2019)
- [3] Caesar, H., Bankiti, V., Lang, A.H., Vora, S., Liong, V.E., Xu, Q., Krishnan, A., Pan, Y., Baldan, G., Beijbom, O.: nuscenes: A multimodal dataset for autonomous driving. In: Proc. IEEE Conference on Computer Vision and Pattern Recognition (CVPR). pp. 11618–11628 (2020)
- [4] Carion, N., Massa, F., Synnaeve, G., Usunier, N., Kirillov, A., Zagoruyko, S.: End-to-end object detection with transformers. In: Proc. European Conference on Computer Vision (ECCV). Lecture Notes in Computer Science, vol. 12346, pp. 213–229 (2020)
- [5] Chen, D., Wang, D., Darrell, T., Ebrahimi, S.: Contrastive test-time adaptation. In: Proc. IEEE Conference on Computer Vision and Pattern Recognition (CVPR). pp. 295–305 (2022)
- [6] Chen, Z., Luo, Y., Wang, Z., Baktashmotlagh, M., Huang, Z.: Revisiting domain-adaptive 3d object detection by reliable, diverse and class-balanced pseudo-labeling. In: Proc. International Conference on Computer Vision (ICCV). pp. 3691–3703 (2023)
- [7] DeBortoli, R., Li, F., Kapoor, A., Hollinger, G.A.: Adversarial training on point clouds for sim-to-real 3d object detection. *IEEE Robotics and Automation Letters* **6**(4), 6662–6669 (2021)
- [8] Deng, B., Qi, C.R., Najibi, M., Funkhouser, T.A., Zhou, Y., Anguelov, D.: Revisiting 3d object detection from an egocentric perspective. In: Proc. Annual Conference on Neural Information Processing (NeurIPS). pp. 26066–26079 (2021)
- [9] Dinu, M., Holzleitner, M., Beck, M., Nguyen, H.D., Huber, A., Eghbal-zadeh, H., Moser, B.A., Pereverzyev, S.V., Hochreiter, S., Zellinger, W.: Addressing parameter choice issues in unsupervised domain adaptation by aggregation. In: Proc. International Conference on Learning Representations (ICLR) (2023)
- [10] Dong, Y., Kang, C., Zhang, J., Zhu, Z., Wang, Y., Yang, X., Su, H., Wei, X., Zhu, J.: Benchmarking robustness of 3d object detection to common corruptions in autonomous driving. In: Proc. IEEE Conference on Computer Vision and Pattern Recognition (CVPR). pp. 1022–1032 (2023)
- [11] Ganin, Y., Ustinova, E., Ajakan, H., Germain, P., Larochelle, H., Laviolette, F., Marchand, M., Lempitsky, V.S.: Domain-adversarial training of neural networks. *Journal of Machine Learning Research* **17**, 59:1–59:35 (2016)
- [12] Geiger, A., Lenz, P., Urtasun, R.: Are we ready for autonomous driving? the KITTI vision benchmark suite. In: Proc. IEEE Conference on Computer Vision and Pattern Recognition (CVPR). pp. 3354–3361 (2012)
- [13] Gong, T., Jeong, J., Kim, T., Kim, Y., Shin, J., Lee, S.J.: Note: Robust continual test-time adaptation against temporal correlation. In: Proc. Annual Conference on Neural Information Processing (NeurIPS). pp. 27253–27266 (2022)
- [14] Gong, T., Kim, Y., Lee, T., Chottananurak, S., Lee, S.J.: Sotta: Robust test-time adaptation on noisy data streams. In: Proc. Annual Conference on Neural Information Processing (NeurIPS) (2024)

- [15] Goyal, S., Sun, M., Raghunathan, A., Kolter, J.Z.: Test time adaptation via conjugate pseudo-labels. In: Proc. Annual Conference on Neural Information Processing (NeurIPS) (2022)
- [16] Gu, Q., Zhou, Q., Xu, M., Feng, Z., Cheng, G., Lu, X., Shi, J., Ma, L.: PIT: position-invariant transform for cross-fov domain adaptation. In: Proc. International Conference on Computer Vision (ICCV). pp. 8741–8750 (2021)
- [17] Hahner, M., Sakaridis, C., Bijelic, M., Heide, F., Yu, F., Dai, D., Gool, L.V.: Lidar snowfall simulation for robust 3d object detection. In: Proc. IEEE Conference on Computer Vision and Pattern Recognition (CVPR). pp. 16343–16353 (2022)
- [18] Hayes, T.L., Kafle, K., Shrestha, R., Acharya, M., Kanan, C.: REMIND your neural network to prevent catastrophic forgetting. In: Proc. European Conference on Computer Vision (ECCV). vol. 12353, pp. 466–483 (2020)
- [19] Hegde, D., Kilic, V., Sindagi, V., Cooper, A.B., Foster, M., Patel, V.M.: Source-free unsupervised domain adaptation for 3d object detection in adverse weather. In: Proc. International Conference on Robotics and Automation (ICRA) (2023)
- [20] Hong, J., Lyu, L., Zhou, J., Spranger, M.: Mecta: Memory-economic continual test-time model adaptation. In: Proc. International Conference on Learning Representations (ICLR) (2023)
- [21] Hu, W., Lin, Z., Liu, B., Tao, C., Tao, Z., Ma, J., Zhao, D., Yan, R.: Overcoming catastrophic forgetting for continual learning via model adaptation. In: Proc. International Conference on Learning Representations (ICLR) (2019)
- [22] Huang, C., Abdelzad, V., Sedwards, S., Czarnecki, K.: Soap: Cross-sensor domain adaptation for 3d object detection using stationary object aggregation pseudo-labelling. In: Proc. Winter Conference on Applications of Computer Vision (WACV) (2024)
- [23] Jung, S., Lee, J., Kim, N., Shaban, A., Boots, B., Choo, J.: Cafa: Class-aware feature alignment for test-time adaptation. In: Proc. International Conference on Computer Vision (ICCV). pp. 19060–19071 (2023)
- [24] Kang, Z., Peng, C., Cheng, Q.: Robust pca via nonconvex rank approximation. In: Proc. International Conference on Data Mining (ICDM). pp. 211–220. IEEE (2015)
- [25] Kemker, R., McClure, M., Abitino, A., Hayes, T.L., Kanan, C.: Measuring catastrophic forgetting in neural networks. In: Proc. Conference on Artificial Intelligence (AAAI). pp. 3390–3398 (2018)
- [26] Kirkpatrick, J., Pascanu, R., Rabinowitz, N., Veness, J., Desjardins, G., Rusu, A.A., Milan, K., Quan, J., Ramalho, T., Grabska-Barwinska, A., et al.: Overcoming catastrophic forgetting in neural networks. In: Proc. National Academy of Sciences (PNAS). pp. 3521–3526 (2017)
- [27] Kong, L., Liu, Y., Li, X., Chen, R., Zhang, W., Ren, J., Pan, L., Chen, K., Liu, Z.: Robo3d: Towards robust and reliable 3d perception against corruptions. In: Proc. International Conference on Computer Vision (ICCV). pp. 19937–19949 (2023)
- [28] Lang, A.H., Vora, S., Caesar, H., Zhou, L., Yang, J., Beijbom, O.: Pointpillars: Fast encoders for object detection from point clouds. In: Proc. IEEE Conference on Computer Vision and Pattern Recognition (CVPR). pp. 12697–12705 (2019)
- [29] Lee, S., Kim, J., Jun, J., Ha, J., Zhang, B.: Overcoming catastrophic forgetting by incremental moment matching. In: Proc. Annual Conference on Neural Information Processing (NeurIPS). pp. 4652–4662 (2017)
- [30] Lehner, A., Gasperini, S., Marcos-Ramiro, A., Schmidt, M., Mahani, M.N., Navab, N., Busam, B., Tombari, F.: 3d-vfield: Adversarial augmentation of point clouds for domain generalization in 3d object detection. In: Proc. IEEE Conference on Computer Vision and Pattern Recognition (CVPR). pp. 17274–17283 (2022)
- [31] Li, B., Ouyang, W., Sheng, L., Zeng, X., Wang, X.: GS3D: an efficient 3d object detection framework for autonomous driving. In: Proc. IEEE Conference on Computer Vision and Pattern Recognition (CVPR). pp. 1019–1028 (2019)

- [32] Li, Z., Guo, J., Cao, T., Liu, B., Yang, W.: GPA-3D: geometry-aware prototype alignment for unsupervised domain adaptive 3d object detection from point clouds. In: Proc. International Conference on Computer Vision (ICCV). pp. 6371–6380 (2023)
- [33] Li, Z., Yao, Y., Quan, Z., Qi, L., Feng, Z., Yang, W.: Adaptation via proxy: Building instance-aware proxy for unsupervised domain adaptive 3d object detection. *IEEE Transactions on Intelligent Vehicles* (2023)
- [34] Luo, Y., Chen, Z., Fang, Z., Zhang, Z., Baktashmotlagh, M., Huang, Z.: Kecor: Kernel coding rate maximization for active 3d object detection. In: Proc. International Conference on Computer Vision (ICCV). pp. 18233–18244 (2023)
- [35] Luo, Z., Cai, Z., Zhou, C., Zhang, G., Zhao, H., Yi, S., Lu, S., Li, H., Zhang, S., Liu, Z.: Unsupervised domain adaptive 3d detection with multi-level consistency. In: Proc. International Conference on Computer Vision (ICCV). pp. 8846–8855 (2021)
- [36] Mao, J., Shi, S., Wang, X., Li, H.: 3d object detection for autonomous driving: A comprehensive survey. *International Journal of Computer Vision* pp. 1–55 (2023)
- [37] McCrae, S., Zakhor, A.: 3d object detection for autonomous driving using temporal lidar data. In: Proc. International Conference on Image Processing (ICIP). pp. 2661–2665 (2020)
- [38] Meyer, G.P., Laddha, A., Kee, E., Vallespi-Gonzalez, C., Wellington, C.K.: Lasernet: An efficient probabilistic 3d object detector for autonomous driving. In: Proc. IEEE Conference on Computer Vision and Pattern Recognition (CVPR). pp. 12677–12686 (2019)
- [39] Mirza, M.J., Micorek, J., Possegger, H., Bischof, H.: The norm must go on: Dynamic unsupervised domain adaptation by normalization. In: Proc. IEEE Conference on Computer Vision and Pattern Recognition (CVPR). pp. 14745–14755. IEEE (2022)
- [40] Montes, H.A., Louedec, J.L., Cielniak, G., Duckett, T.: Real-time detection of broccoli crops in 3d point clouds for autonomous robotic harvesting. In: Proc. International Conference on Intelligent Robots and Systems (IROS). pp. 10483–10488 (2020)
- [41] Nejjar, I., Wang, Q., Fink, O.: DARE-GRAM : Unsupervised domain adaptation regression by aligning inverse gram matrices. In: Proc. IEEE Conference on Computer Vision and Pattern Recognition (CVPR). pp. 11744–11754 (2023)
- [42] Nguyen, A.T., Nguyen-Tang, T., Lim, S.N., Torr, P.H.: Tipi: Test time adaptation with transformation invariance. In: Proc. IEEE Conference on Computer Vision and Pattern Recognition (CVPR). pp. 24162–24171 (June 2023)
- [43] Niloy, F.F., Ahmed, S.M., Raychaudhuri, D.S., Oymak, S., Roy-Chowdhury, A.K.: Effective restoration of source knowledge in continual test time adaptation. In: Proc. Winter Conference on Applications of Computer Vision (WACV). pp. 2091–2100 (2024)
- [44] Niu, S., Wu, J., Zhang, Y., Chen, Y., Zheng, S., Zhao, P., Tan, M.: Efficient test-time model adaptation without forgetting. In: Proc. International Conference on Machine Learning (ICML). pp. 16888–16905 (2022)
- [45] Niu, S., Wu, J., Zhang, Y., Wen, Z., Chen, Y., Zhao, P., Tan, M.: Towards stable test-time adaptation in dynamic wild world. In: Proc. International Conference on Learning Representations (ICLR) (2023)
- [46] Peng, X., Zhu, X., Ma, Y.: CL3D: unsupervised domain adaptation for cross-lidar 3d detection. In: Proc. Conference on Artificial Intelligence (AAAI). pp. 2047–2055 (2023)
- [47] Qian, R., Lai, X., Li, X.: 3d object detection for autonomous driving: A survey. *Pattern Recognition* **130**, 108796 (2022)
- [48] Recht, B., Fazel, M., Parrilo, P.A.: Guaranteed minimum-rank solutions of linear matrix equations via nuclear norm minimization. *SIAM review* **52**(3), 471–501 (2010)

- [49] Rist, C.B., Enzweiler, M., Gavrila, D.M.: Cross-sensor deep domain adaptation for lidar detection and segmentation. In: Proc. Intelligent Vehicles Symposium, (IV). pp. 1535–1542 (2019)
- [50] Saleh, K., Abobakr, A., Attia, M.H., Iskander, J., Nahavandi, D., Hossny, M., Nahavandi, S.: Domain adaptation for vehicle detection from bird’s eye view lidar point cloud data. In: Proc. International Conference on Computer Vision (ICCV). pp. 3235–3242 (2019)
- [51] Saltori, C., Lathuilière, S., Sebe, N., Ricci, E., Galasso, F.: Sf-uda<sup>3d</sup>: Source-free unsupervised domain adaptation for lidar-based 3d object detection. In: Proc. International Conference on 3D Vision (3DV). pp. 771–780 (2020)
- [52] Shi, S., Guo, C., Jiang, L., Wang, Z., Shi, J., Wang, X., Li, H.: PV-RCNN: point-voxel feature set abstraction for 3d object detection. In: Proc. IEEE Conference on Computer Vision and Pattern Recognition (CVPR). pp. 10526–10535 (2020)
- [53] Song, J., Lee, J., Kweon, I.S., Choi, S.: Ecotta: Memory-efficient continual test-time adaptation via self-distilled regularization. In: Proc. IEEE Conference on Computer Vision and Pattern Recognition (CVPR). pp. 11920–11929 (2023)
- [54] Stewart, R., Andriluka, M., Ng, A.Y.: End-to-end people detection in crowded scenes. In: Proc. IEEE Conference on Computer Vision and Pattern Recognition (CVPR). pp. 2325–2333 (2016)
- [55] Sun, P., Kretschmar, H., Dotiwalla, X., Chouard, A., Patnaik, V., Tsui, P., Guo, J., Zhou, Y., Chai, Y., Caine, B., Vasudevan, V., Han, W., Ngiam, J., Zhao, H., Timofeev, A., Ettinger, S., Krivokon, M., Gao, A., Joshi, A., Zhang, Y., Shlens, J., Chen, Z., Anguelov, D.: Scalability in perception for autonomous driving: Waymo open dataset. In: Proc. IEEE Conference on Computer Vision and Pattern Recognition (CVPR). pp. 2443–2451 (2020)
- [56] Team, O.D.: Openpcdet: An open-source toolbox for 3d object detection from point clouds. <https://github.com/open-mmlab/OpenPCDet> (2020)
- [57] Tomar, D., Vray, G., Bozorgtabar, B., Thiran, J.: Tesla: Test-time self-learning with automatic adversarial augmentation. In: Proc. IEEE Conference on Computer Vision and Pattern Recognition (CVPR). pp. 20341–20350 (2023)
- [58] Tomar, D., Vray, G., Bozorgtabar, B., Thiran, J.P.: Tesla: Test-time self-learning with automatic adversarial augmentation. In: Proc. IEEE Conference on Computer Vision and Pattern Recognition (CVPR). pp. 20341–20350 (2023)
- [59] Tsai, D., Berrio, J.S., Shan, M., Nebot, E., Worrall, S.: Ms3d++: Ensemble of experts for multi-source unsupervised domain adaption in 3d object detection. CoRR **abs/2308.05988** (2023)
- [60] Tsai, D., Berrio, J.S., Shan, M., Nebot, E.M., Worrall, S.: Viewer-centred surface completion for unsupervised domain adaptation in 3d object detection. In: Proc. International Conference on Robotics and Automation (ICRA). pp. 9346–9353 (2023)
- [61] VS, V., Oza, P., Patel, V.M.: Towards online domain adaptive object detection. In: Proc. Winter Conference on Applications of Computer Vision (WACV). pp. 478–488 (2023)
- [62] Wang, D., Shelhamer, E., Liu, S., Olshausen, B.A., Darrell, T.: Tent: Fully test-time adaptation by entropy minimization. In: Proc. International Conference on Learning Representations (ICLR) (2021)
- [63] Wang, J., Lan, S., Gao, M., Davis, L.S.: Infofocus: 3d object detection for autonomous driving with dynamic information modeling. In: Proc. European Conference on Computer Vision (ECCV). vol. 12355, pp. 405–420. Springer (2020)
- [64] Wang, Q., Fink, O., Gool, L.V., Dai, D.: Continual test-time domain adaptation. In: Proc. IEEE Conference on Computer Vision and Pattern Recognition (CVPR). pp. 7191–7201 (2022)

- [65] Wang, S., Zhang, D., Yan, Z., Zhang, J., Li, R.: Feature alignment and uniformity for test time adaptation. In: Proc. IEEE Conference on Computer Vision and Pattern Recognition (CVPR). pp. 20050–20060 (2023)
- [66] Wang, Y., Chao, W., Garg, D., Hariharan, B., Campbell, M.E., Weinberger, K.Q.: Pseudo-lidar from visual depth estimation: Bridging the gap in 3d object detection for autonomous driving. In: Proc. IEEE Conference on Computer Vision and Pattern Recognition (CVPR). pp. 8445–8453 (2019)
- [67] Wang, Y., Chen, X., You, Y., Li, L.E., Hariharan, B., Campbell, M.E., Weinberger, K.Q., Chao, W.: Train in germany, test in the USA: making 3d object detectors generalize. In: Proc. IEEE Conference on Computer Vision and Pattern Recognition (CVPR). pp. 11710–11720 (2020)
- [68] Wang, Z., Luo, Y., Zheng, L., Chen, Z., Wang, S., Huang, Z.: In search of lost online test-time adaptation: A survey. CoRR **abs/2310.20199** (2023)
- [69] Wei, Y., Wei, Z., Rao, Y., Li, J., Zhou, J., Lu, J.: Lidar distillation: Bridging the beam-induced domain gap for 3d object detection. In: Proc. European Conference on Computer Vision (ECCV). vol. 13699, pp. 179–195 (2022)
- [70] Xu, Q., Zhou, Y., Wang, W., Qi, C.R., Anguelov, D.: SPG: unsupervised domain adaptation for 3d object detection via semantic point generation. In: Proc. International Conference on Computer Vision (ICCV). pp. 15426–15436 (2021)
- [71] Yan, Y., Mao, Y., Li, B.: SECOND: sparsely embedded convolutional detection. Sensors **18**(10), 3337 (2018)
- [72] Yang, J., Shi, S., Wang, Z., Li, H., Qi, X.: ST3D: self-training for unsupervised domain adaptation on 3d object detection. In: Proc. IEEE Conference on Computer Vision and Pattern Recognition (CVPR). pp. 10368–10378 (2021)
- [73] Yang, J., Shi, S., Wang, Z., Li, H., Qi, X.: St3d++: denoised self-training for unsupervised domain adaptation on 3d object detection. IEEE Transactions on Pattern Analysis and Machine Intelligence (2022)
- [74] Ye, C., Qian, X.: 3-d object recognition of a robotic navigation aid for the visually impaired. IEEE Transactions on Neural Systems and Rehabilitation Engineering **26**(2), 441–450 (2018)
- [75] Yin, T., Zhou, X., Krähenbühl, P.: Center-based 3d object detection and tracking. In: Proc. IEEE Conference on Computer Vision and Pattern Recognition (CVPR). pp. 11784–11793 (2021)
- [76] You, Y., Diaz-Ruiz, C.A., Wang, Y., Chao, W., Hariharan, B., Campbell, M.E., Weinberger, K.Q.: Exploiting playbacks in unsupervised domain adaptation for 3d object detection in self-driving cars. In: Proc. International Conference on Robotics and Automation (ICRA). pp. 5070–5077 (2022)
- [77] You, Y., Wang, Y., Chao, W., Garg, D., Pleiss, G., Hariharan, B., Campbell, M.E., Weinberger, K.Q.: Pseudo-lidar++: Accurate depth for 3d object detection in autonomous driving. In: Proc. International Conference on Learning Representations (ICLR) (2020)
- [78] Yuan, L., Xie, B., Li, S.: Robust test-time adaptation in dynamic scenarios. In: Proc. IEEE Conference on Computer Vision and Pattern Recognition (CVPR). pp. 15922–15932 (2023)
- [79] Yuen, K.K.F.: Inverse gram matrix methods for prioritization in analytic hierarchy process: Explainability of weighted least squares optimization method. CoRR **abs/2401.01190** (2024)
- [80] Zeng, L., Han, J., Du, L., Ding, W.: Rethinking precision of pseudo label: Test-time adaptation via complementary learning. Pattern Recognition Letters **177**, 96–102 (2024)
- [81] Zeng, Y., Wang, C., Wang, Y., Xu, H., Ye, C., Yang, Z., Ma, C.: Learning transferable features for point cloud detection via 3d contrastive co-training. In: Proc. Annual Conference on Neural Information Processing (NeurIPS). pp. 21493–21504 (2021)
- [82] Zhang, M., Levine, S., Finn, C.: MEMO: test time robustness via adaptation and augmentation. In: Proc. Annual Conference on Neural Information Processing (NeurIPS) (2022)

- [83] Zhang, W., Li, W., Xu, D.: SRDAN: scale-aware and range-aware domain adaptation network for cross-dataset 3d object detection. In: Proc. IEEE Conference on Computer Vision and Pattern Recognition (CVPR). pp. 6769–6779 (2021)
- [84] Zhao, B., Chen, C., Xia, S.T.: Delta: degradation-free fully test-time adaptation. In: Proc. International Conference on Learning Representations (ICLR) (2023)
- [85] Zhou, Z., Li, L., Fürsterling, A., Durocher, H.J., Mouridsen, J., Zhang, X.: Learning-based object detection and localization for a mobile robot manipulator in SME production. *Robotics and Computer-Integrated Manufacturing* **73**, 102229 (2022)

## A Appendix / Supplemental Material

In this supplementary material, we include Algorithm 1: detailed algorithm of the proposed method, Sec. A.1: implementation details on computing devices, hyperparameter selection, data augmentations, pseudo-labeling, baseline losses and ensemble techniques in MOS, Sec. A.2: more experimental results and analysis across multiple classes to address both cross-dataset and cross-corruption shifts, Sec. A.3: visualized 3D boxes predicted by checkpoints with different synergy weights, Sec. A.4: experimental results with different backbone detector, and Sec. A.5: complexity analysis of the proposed method, including time and memory usage.

### A.1 Implementation Details

Our code is developed on the OpenPCDet [56] point cloud detection framework, and operates on a single NVIDIA RTX A6000 GPU with 48 GB of memory. We choose a batch size of 8, and set hyperparameters  $L = 112$  across all experiments. We set the model bank size of  $K = 5$  to balance performance and memory usage. For evaluation, we use the KITTI benchmark’s official metrics, reporting average precision for car class in both 3D (*i.e.*,  $AP_{3D}$ ) and bird’s eye view (*i.e.*,  $AP_{BEV}$ ), over 40 recall positions, with a 0.7 IoU threshold. We set  $S_{feat}$  to a small positive value  $\epsilon = 0.01$  once  $\text{rank}(\cdot)$  reaches  $D$ , to ensure  $\tilde{\mathbf{G}}$  is invertible. The detection model is pretrained using the training set of the source dataset, and subsequently adapted and tested on the validation set of KITTI.

**Augmentations.** We adopt data augmentation strategies from prior studies [73, 72, 35, 6] for methods requiring augmentations, such as MemCLR [61], CoTTA [64], and MOS. While CoTTA suggests employing multiple augmentations, our empirical results indicate that for TTA-3OD, utilizing only a single random world scaling enhances performance, whereas additional augmentations diminish it. Consequently, following the approach [35], we implement random world scaling for the mean-teacher baselines, applying strong augmentation (scaling between 0.9 and 1.1) and weak augmentation (scaling between 0.95 and 1.05) for all test-time domain adaptation tasks.

**Pseudo-labeling.** We directly apply the pseudo-labeling strategies from [72, 73] to CoTTA and MOS for self-training, using the default configurations.

**Baseline Losses.** For Tent [62] and SAR [45], which calculate the entropy minimization loss, we sum the losses based on classification logits for all proposals from the first detection stage. For MemCLR [61], we integrate its implementation into 3D detectors by reading/writing pooled region of interest (RoI) features extracted from the second detection stage, and compute the memory contrastive loss. For all baseline methods, we use default hyperparameters from their implementation code.

**Ensemble Details and Memory Optimization in MOS.** In the proposed MOS, we optimize memory usage by sequentially loading each checkpoint from the hard disk onto the GPU, extracting the outputted intermediate feature maps and box predictions needed for calculating the gram matrix and synergy weights. After saving the outputs for the currently loaded checkpoint, we remove it from the GPU before loading the next one. Once the synergy weights are calculated, in the model assembly process, we again sequentially load checkpoints, multiplying each model’s parameters by the corresponding synergy weight and aggregate them into the supermodel. We report the optimized memory usage in Fig. 8.

### A.2 Experimental Results Across Multiple Classes

**Cross-Dataset Shifts.** We conduct experiments to evaluate the proposed test-time adaptation method across various datasets for multiple object classes. As shown in Tab. 3, our proposed MOS consistently surpasses all test-time adaptation (TTA) baselines in  $AP_{BEV}$  for every class. Specifically, in the Waymo  $\rightarrow$  KITTI task, MOS exceeds the leading baseline (CoTTA) by 3.3% for pedestrians and 2.6% for cyclists in  $AP_{3D}$ . For the more challenging nuScenes  $\rightarrow$  KITTI adaptation, which faces a significant environmental shift (beam numbers: 32 vs. 64), MOS significantly outperforms CoTTA by 4.9% for pedestrians and 31.5% for cyclists, highlighting CoTTA’s limitations with more severe domain shifts. Notably, MOS also surpasses the unsupervised domain adaptive (UDA) 3D object detection method (ST3D) by 11.4% in the cyclist class for the task of Waymo  $\rightarrow$  KITTI, demonstrating its effectiveness across all object classes and competitive performance against the UDA approach.



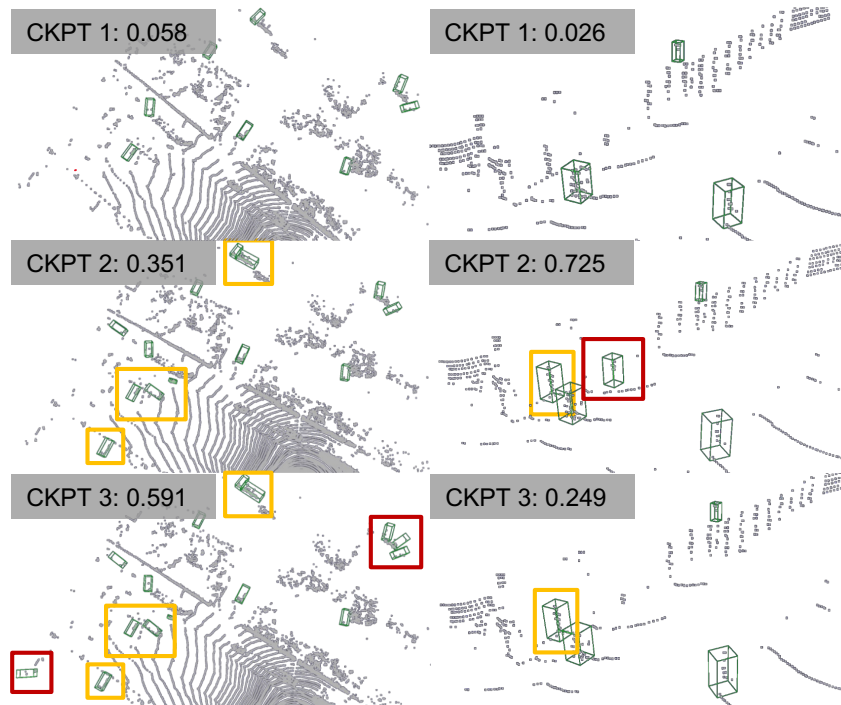


Figure 7: Visualization of box predictions from different checkpoints in the model bank of size  $K = 3$ , with corresponding synergy weight. These checkpoints are selected and stored in the model bank with the proposed MOS when adapting the 3D detector [71] pre-trained on Waymo [55], to the KITTI [12] dataset at test-time. Objects uniquely detected by only one checkpoint are marked in **red**, while those detected by two checkpoints are marked in **yellow**.

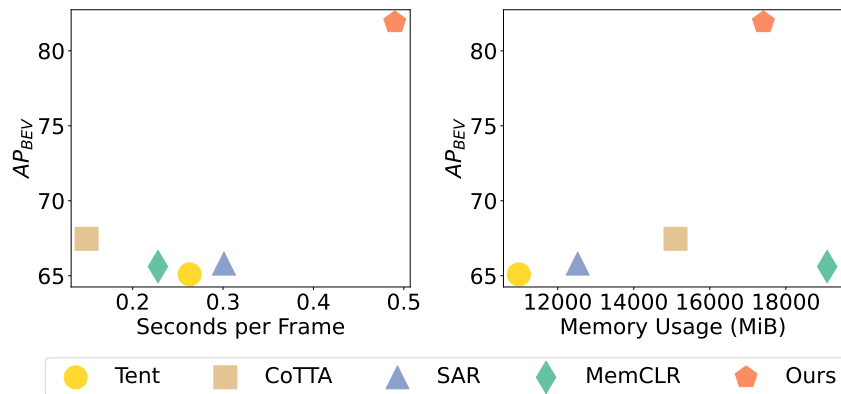


Figure 8: Time and memory usage of method implementations when adapting the 3D detector [71] pre-trained on Waymo [55], to the KITTI [12] dataset at test-time.  $AP_{BEV}$  is reported.

**Cross-Corruption Shifts.** Our experiments further explore adapting to 3D scenes under the challenging cross-corruption shifts for pedestrian and cyclist classes. As shown in Tab. 4, our MOS method surpasses all baselines across most corruptions, achieving the highest mean  $AP_{3D}$ : 40.41, 36.26 and 33.24 in easy, moderate and hard difficulty, respectively. However, for motion blur, beam missing, and cross sensor, the effectiveness of pseudo-labelling methods such as CoTTA and MOS is reduced. This is due to the small size and rareness of pedestrian objects, which lead to less accurate pseudo labels. For cyclists, which are slightly larger objects than pedestrians, CoTTA improves  $AP_{3D}$  in motion blur scenarios (CoTTA’s 31.18 vs. MemCLR’s 29.75) but still struggles with harder corruptions including cross sensor and beam missing, as indicated in Table 5. Conversely, MOS effec-

Table 3: [Complete Results] Cross-dataset results in moderate difficulty across multiple classes. We report average precision (AP) for bird’s-eye view ( $AP_{BEV}$ ) / 3D ( $AP_{3D}$ ) of **car**, **pedestrian**, and **cyclist** with IoU threshold set to 0.7, 0.5, and 0.5 respectively. The last column shows the mean AP for all classes. We indicate the best adaptation result by **bold**, and the highlighted row represents the proposed method.

Task	Method	Car	Pedestrian	Cyclist
Waymo → KITTI	No Adapt.	67.64 / 27.48	46.29 / 43.13	48.61 / 43.84
	SN [67]	78.96 / 59.20	53.72 / 50.44	44.61 / 41.43
	ST3D [72]	82.19 / 61.83	52.92 / 48.33	53.73 / 46.09
	Oracle	83.29 / 73.45	46.64 / 41.33	62.92 / 60.32
	Tent [62]	65.09 / 30.12	46.21 / 43.24	46.59 / 41.72
	CoTTA [64]	67.46 / 35.34	49.02 / 45.03	<b>55.31</b> / 50.07
	SAR [45]	65.81 / 30.39	47.99 / 44.72	47.14 / 41.17
	MemCLR [61]	65.61 / 29.83	48.25 / 44.84	47.49 / 41.67
	<b>MOS</b>	<b>81.90 / 64.16</b>	<b>50.25 / 46.51</b>	54.12 / <b>51.36</b>
nuScenes → KITTI	No Adapt.	51.84 / 17.92	39.95 / 34.57	17.61 / 11.17
	SN [67]	40.03 / 21.23	38.91 / 34.36	11.11 / 5.67
	ST3D [72]	75.94 / 54.13	44.00 / 42.60	29.58 / 21.21
	Oracle	83.29 / 73.45	46.64 / 41.33	62.92 / 60.32
	Tent [62]	46.90 / 18.83	39.69 / 35.53	19.64 / 10.49
	CoTTA [64]	68.81 / 47.61	40.90 / 36.64	20.68 / 13.81
	SAR [45]	65.81 / 30.39	39.78 / 35.63	19.56 / 10.26
	MemCLR [61]	65.61 / 29.83	40.31 / 35.14	19.21 / 9.66
	<b>MOS</b>	<b>71.13 / 51.11</b>	<b>42.94 / 38.45</b>	<b>21.65 / 18.16</b>

Table 4: TTA-3OD results (easy/moderate/hard  $AP_{3D}$ ) of **pedestrian** class under the cross-corruption scenario (Waymo → KITTI-C) at heavy corruption level.

	No Adaptation	Tent [62]	CoTTA [64]	SAR [45]	MemCLR [61]	<b>MOS</b>
Fog	30.48/26.15/23.61	31.22/26.68/23.99	31.29/26.69/24.05	30.68/25.94/23.70	30.51/26.02/23.77	<b>32.38/27.51/24.85</b>
Wet.	49.10/44.44/41.74	49.13/44.58/41.85	49.14/45.01/42.23	49.18/44.59/41.97	49.09/44.55/41.81	<b>51.34/46.88/43.16</b>
Snow	47.22/42.26/39.19	47.55/42.79/39.44	46.30/41.62/38.11	47.42/42.85/39.54	47.68/42.78/39.45	<b>49.42/44.82/40.79</b>
Moti.	27.18/25.02/23.29	27.47/25.25/23.43	27.28/25.43/23.41	27.34/25.15/23.31	27.44/25.19/23.36	<b>27.54/25.93/23.86</b>
Beam.	32.47/27.89/25.27	34.50/30.55/28.18	32.22/27.41/25.13	<b>34.83/30.74/28.54</b>	34.53/30.30/28.16	34.02/29.73/27.35
CrossT.	47.42/43.08/40.37	47.66/43.37/40.51	47.76/43.29/40.39	48.13/43.65/40.71	47.87/43.58/40.48	<b>50.78/45.42/41.73</b>
Inc.	49.28/44.79/42.21	49.18/44.80/42.11	49.36/45.39/42.77	49.22/44.70/42.24	49.01/44.76/42.11	<b>51.06/46.83/43.31</b>
CrossS.	22.46/18.40/16.08	27.70/22.82/20.30	22.11/17.88/15.98	<b>27.99/23.20/21.36</b>	27.23/23.70/21.63	26.74/22.94/20.89
Mean	38.20/34.00/31.47	39.30/35.11/32.48	38.18/34.09/31.52	39.35/35.10/32.67	39.17/35.11/32.60	<b>40.41/36.26/33.24</b>

tively addresses both cross sensor and beam missing challenges for cyclists, demonstrating superior results: 14.9% and 18.6% higher than the best-performing baseline, respectively. Despite pseudo labelling’s limitations with rare and small-sized objects under severe corruptions, MOS presents a comparable test-time adaptation ability for pedestrian objects and shows the leading performance for cyclists, demonstrating the effectiveness of leveraging diverse category knowledge from historical checkpoints.

### A.3 Visualization of Synergy Weights

In Fig. 7, we visualize the predicted point clouds from different checkpoints in a bank  $\mathbf{F}$  of size  $K = 3$ , each annotated with its synergy weight (SW) by Eq. (5). We note that CKPT 2 detects more pedestrians (row 2, column 2) that are overlooked by others. To capture this knowledge, the proposed MOS assigns CKPT 2 with a higher SW when inferring the right point cloud (column 2). However, for inferring the left point cloud (column 1), CKPT 2 fails to localize the car detected by CKPT 3, resulting in CKPT 3 receiving a higher SW than CKPT 2. Regarding CKPT 1, since other checkpoints cover all its box predictions, it is assigned the lowest SW to minimize redundancy. Therefore, for each input point cloud, the proposed MOS employs a separate strategy (*i.e.*, weighted averaging by SW) to combine checkpoints, ensuring the acquisition of non-redundant, long-term knowledge from historical checkpoints.

Table 5: TTA-3OD results (easy/moderate/hard AP<sub>3D</sub>) of **cyclist** class under the cross-corruption scenario (Waymo → KITTI-C) at heavy corruption level.

	No Adaptation	Tent [62]	CoTTA [64]	SAR [45]	MemCLR [61]	MOS
Fog	21.15/17.91/16.66	23.62/19.21/18.33	22.60/18.74/17.57	23.49/19.02/18.10	23.43/19.01/17.86	<b>25.62/21.34/20.10</b>
Wet.	60.36/49.61/47.20	59.72/48.57/45.96	61.36/49.27/47.04	57.43/46.48/43.96	57.76/46.34/44.79	<b>64.73/52.11/49.60</b>
Snow	48.87/40.37/37.96	52.81/42.25/40.11	52.91/41.55/39.09	52.09/41.89/39.26	52.24/41.71/39.28	<b>57.12/45.53/43.39</b>
Moti.	34.62/29.25/27.33	36.79/29.04/27.31	40.37/31.18/29.34	37.53/29.78/28.12	38.19/29.75/28.19	<b>43.90/34.63/32.87</b>
Beam.	32.48/22.42/21.26	36.08/25.03/23.85	30.89/21.37/20.42	37.16/26.21/24.74	36.34/25.35/24.32	<b>43.06/30.19/28.43</b>
CrossT.	59.56/48.75/46.20	58.72/49.26/46.51	62.14/49.13/46.21	58.66/49.16/46.61	58.68/48.87/46.40	<b>65.10/51.67/49.30</b>
Inc.	59.62/49.03/46.82	59.14/47.87/45.11	59.89/47.62/45.44	58.86/47.93/45.51	58.91/48.28/45.68	<b>60.55/49.57/47.23</b>
CrossS.	18.38/11.40/10.93	24.84/15.04/14.66	20.98/12.77/12.28	26.19/15.29/14.95	25.46/15.06/14.49	<b>30.34/18.66/17.73</b>
Mean	41.88/33.59/31.79	43.96/34.53/32.73	43.89/33.95/32.17	43.93/34.47/32.66	43.88/34.30/32.63	<b>48.80/37.96/36.08</b>

---

### Algorithm 1 The Proposed Model Synergy for TTA-3OD

---

**Input:**  $f_0$ : source pretrained model,  $\{x_t\}_{t=1}^T$ : point clouds to test,  $\mathbf{F}$ : model bank.

**Output:**  $f_t$ : model adapted to the target point clouds.

**Phase 1: Warm-up.**

Start self-training with  $f_0$ , and add each of trained  $f_t$  into  $\mathbf{F}$  until reaching capacity.

**Phase 2: Model Synergy.**

**for** each remaining batch  $x_t$  **do**

    Calculate the inverse of generalized Gram matrix  $\tilde{\mathbf{G}}^{-1}$ , via Eq. (5) (8) (9) (10)

    Calculate synergy weights  $\tilde{\mathbf{w}}$  with  $\tilde{\mathbf{G}}^{-1}$ , for each of model in  $\mathbf{F}$ , via Eq. (5)

    Assemble models within  $\mathbf{F}$  weighted by  $\tilde{\mathbf{w}}$ , into a super model  $f_t^*$ , via Eq. (6)

    Generate prediction for  $x_t$  as pseudo label  $\hat{\mathbf{B}}^t$  by  $f_t^*$ , to train the current model  $f_t$ , via Eq. (7)

**Phase 3: Model Bank Update.**

**for** each time of training/infering  $L$  online batches **do**

        Calculate the mean synergy weights  $\bar{\mathbf{w}}$ , via Eq. (11)

        Remove the most redundant model in  $\mathbf{F}$  and add  $f_t$  into  $\mathbf{F}$ , via Eq. (12)

**end for**

**end for**

---

## A.4 Sensitivity to 3D Backbone Detector

We evaluate the sensitivity of the proposed MOS when integrated with a different two-stage, point- and voxel-based backbone detector: PVRCNN [52]. We report the results of TTA baselines and the MOS for test-time adapting the PVRCNN from Waymo to KITTI in Tab 6. It is observed that the proposed MOS shows a significant performance increase (36.16% in AP<sub>3D</sub>) over the leading baseline CoTTA, demonstrating that our model synergy is model-agnostic and maintains consistent effectiveness across different backbones.

## A.5 Complexity Analysis

This section analyzes the complexity of the proposed MOS. Recall that  $K$  models in the bank  $\mathbf{F}$  infer every test batch  $x_t$  from the datasets  $\{x_t\}_{t=1}^T$ , the theoretical time complexity is asymptotically equivalent to  $\mathcal{O}(T)$ , as  $K$  is a constant. Concerning the space complexity, we assume that a 3D detection network requires  $N_{\text{param}}$  parameters for memory storage, and the space complexity is bounded by  $\mathcal{O}(N_{\text{param}})$ . Theoretically, the proposed MOS exhibits a manageable linear complexity growth with respect to model size and dataset size.

### A.5.1 Time and Memory Usage

In this section, we report the adaptation speed (seconds per frame) and GPU memory usage (MiB) of implemented methods in Fig. 8. It is observed that the proposed MOS significantly outperforms the top baseline, improving AP<sub>3D</sub> by 21.4% while only requiring an additional 0.255 seconds per frame compared to the baseline average. In terms of memory usage, mean-teacher frameworks such as MemCLR (19087 MiB) and CoTTA (15099 MiB) consume more resources as they simultaneously load dual networks in the GPU. The substantial consumption of MemCLR mainly stems from its extra transformer-based memory module. Compared to MemCLR, our MOS maintains a lower memory

Table 6: Results of TTA-3OD on adapting Waymo  $\rightarrow$  KITTI using **PV-RCNN** [52].

TTA Method	No Adapt	Tent [62]	CoTTA [64]	SAR [45]	MemCLR [61]	MOS
AP <sub>BEV</sub> /AP <sub>3D</sub>	63.60/22.01	55.96/27.49	67.85/38.52	59.77/21.33	55.92/15.77	<b>72.60/52.45</b>

footprint at 17411 MiB. Overall, MOS offers substantially superior adaptation performance with a manageable increase in memory and time consumption.